Applied Catalysis B: Environmental 292 (2021) 120183

Contents lists available at ScienceDirect

Applied Catalysis B: Environmental

journal homepage: www.elsevier.com/locate/apcatb

Novel perovskite catalysts for CO_2 utilization - Exsolution enhanced reverse water-gas shift activity

L. Lindenthal [a], J. Popovic [a], R. Rameshan [a], J. Huber [a], F. Schrenk [a], T. Ruh [a], A. Nenning [b], S. Löffler [c], A.K. Opitz [b], C. Rameshan [a,*]

[a] TU Wien, Institute of Materials Chemistry, Getreidemarkt 9/165-PC, 1060, Vienna, Austria
[b] TU Wien, Institute of Chemical Technologies and Analytics, Getreidemarkt 9/164-EC, 1060, Vienna, Austria
[c] TU Wien, USTEM, Wiedner Hauptstr. 8-10, 1040, Vienna, Austria

ARTICLE INFO

Keywords:
Reverse water-gas shift
Perovskites
Exsolution
Nanoparticles
Catalyst design

ABSTRACT

Reverse Water-Gas Shift (rWGS) is among the reactions with the highest readiness level for technological implementation of CO_2 utilization as an abundant and renewable carbon source, and its transformation for instance into synthetic fuels. Hence, great efforts are made in terms of further development and comprehension of novel catalyst materials. To achieve excellent catalytic performance, catalytically active (nano)particles that are evenly distributed on (and ideally embedded in) an active support are crucial.

An extremely versatile material class that exhibits the desired properties are perovskite-type oxides due to the fact that they can easily be doped with highly active elements. Upon controlled reduction or during reaction, these dopants leave the perovskite lattice and diffuse through the material to form nanoparticles at the surface (by exsolution) where they can greatly enhance the activity.

Here, six perovskites were studied and their exsolution capabilities as well as rWGS performance were explored. Nanoparticle exsolution significantly enhanced the rWGS activity, with the catalytic activity being in the order $Nd_{0.6}Ca_{0.4}Fe_{0.9}Co_{0.1}O_{3-\delta}$ > $Nd_{0.6}Ca_{0.4}Fe_{0.9}Ni_{0.1}O_{3-\delta}$ > $Nd_{0.9}Ca_{0.1}FeO_{3-\delta}$ > $Nd_{0.6}Ca_{0.4}FeO_{3-\delta}$ > $La_{0.6}Ca_{0.4}FeO_{3-\delta}$ > $La_{0.9}Ca_{0.1}FeO_{3-\delta}$ > $La_{0.6}Sr_{0.4}FeO_{3-\delta}$(benchmark). Moreover, it could be shown that nanoparticles formed due to exsolution are stable at high reaction temperatures. In this paper, the flexibility of the investigated perovskite materials is demonstrated, on the one hand facilitating a material design approach enabling control over size and composition of exsolved nanoparticles. On the other hand, the studied perovskites offer a tuneable host lattice providing oxygen vacancies for efficient CO_2 adsorption, activation, and resulting interface boundaries with the ability to enhance the catalytic activity.

1. Introduction

A major challenge of our century is the substitution of fossil energy carriers by renewable resources. For chemical industry, the independence from crude oil and coal as carbon source is highly desirable. An alternative, ubiquitous, nontoxic, and sustainable carbon source is CO_2, but the stable nature of the molecule makes catalytic activation essential [1]. Processes which enable activation and chemical conversion of CO_2 require high energy input, desirably provided by renewable sources (e.g. wind, solar, geothermal, etc.). In conjunction with renewable energy, CO_2 has the potential to generate a closed carbon cycle, mitigating CO_2 emissions and the related issue of global warming [2]. Large-scale industrial processes with the currently greatest economic potential for CO_2 utilization are the production of hydrocarbon fuels, methanol, or – for fine chemical production – urea and salicylic acid [3].

Reverse water gas shift reaction (rWGS) is among the most promising technologies to convert CO_2 into synthetic fuels or CO as their precursor (other examples include direct hydrogenation of CO_2 and methane dry reforming – MDR) [4]. For MDR, the high (400 °C–600 °C) operating temperatures and the associated problems of catalyst sintering and coke formation are major drawbacks [5]. Additionally, catalysts are reported to be very sensitive to sulphur impurities, which cause catalyst deactivation [6]. While direct hydrogenation of CO_2 is seen as very promising for methanol synthesis on an industrial scale, as it is thermodynamically more favourable than rWGS [7], the indirect route via rWGS and CO is reported to give a 20 % higher methanol yield compared to direct

* Corresponding author.
E-mail address: christoph.rameshan@tuwien.ac.at (C. Rameshan).

https://doi.org/10.1016/j.apcatb.2021.120183
Received 29 January 2021; Received in revised form 22 March 2021; Accepted 30 March 2021
Available online 3 April 2021

hydrogenation [4]. Furthermore, it has been suggested that rWGS plays a major role in selective methanation of CO_2, and it occurs in Fischer-Tropsch reactors operated with high CO_2 feeds [8]. In summary, rWGS is a very promising reaction for activation and utilization of CO_2, which is the motivation for the present study.

The rWGS reaction is an equilibrium-limited reaction (Eq. (1)) and due to its endothermic nature CO formation is favoured at high temperatures. At lower temperatures, the equilibrium favours the water-gas shift reaction (i.e. reverse of Eq. (1)). Moreover, at lower temperatures methanation is a well-known side reaction [4].

$$H_2 + CO_2 \rightleftharpoons CO + H_2O \ \Delta_r H^\circ_{298} = 42.1 \text{ kJ mol}^{-1} \quad (1)$$

In recent years, a lot of work was dedicated to the improvement of rWGS catalysts or the design of novel materials. The most widely studied materials are supported catalysts based on copper, platinum, or rhodium [9,10]. Copper has the advantage of lower operating temperatures and suppression of methanation. A comparison of supported platinum catalysts and supported iron and copper reveals improved CO_2 conversion rates; however, the selectivity with respect to CO is diminished. [4]. Furthermore, nickel and cobalt based as well as bimetallic catalysts [11,12] were studied. Notably, there is the need for cheap, abundant catalyst materials, as the high cost of noble metals constitutes the major constraint for their large scale application [13]. For instance, Wang et al. showed that the combination of oxygen vacancies and finely dispersed Ni was the reason for the high catalytic activity of their Ni/CeO_2 catalyst [11]. Pastor-Pérez et al. demonstrated high CO_2 conversion levels exclusively to CO under various reaction parameters for doped FeCu catalysts [14]. Also, perovskite based rWGS catalysts were tested for their performance as demonstrated by Kim et al. for barium zirconate-based materials [15] or by Daza et al. for cobalt-based perovskites [16]. Additionally, various promotion elements were investigated, e.g. the enhancement of the catalytic activity with potassium, as studied by Chwen et al. [17]

Among the wide variety of catalysts reviewed in literature, iron-based catalysts have shown the greatest potential, due to their thermal stability and high oxygen mobility [18], while remaining a feasible option in terms of production costs. Ko et al. performed DFT calculations on CO_2 dissociation, finding preferred CO_2 to CO dissociation on Fe-containing bimetallic particles [19], thus, highlighting the potential of iron-based catalysts even further. A further advantage of application of reducible oxides in rWGS is that their enhanced oxygen mobility prevents coking [20].

Perovskite type oxides with the general formula ABO_3 consist of two cations of different sizes (A is larger than B). The wide range of possible structures (many A and B cations can be combined) in conjunction with the option to introduce catalytically active or promoting elements via doping facilitate systematic catalyst development [21]. Moreover, many different types of perovskites have been the subject of extensive research and their properties have been studied thoroughly, particularly because of their wide-spread application in many areas such as solid-state electrochemistry, fuel cell technology, and catalysis [22–24]. Among the desired properties of perovskites are their excellent thermal stability (especially important in solid oxide fuel cells due to the high operation temperatures between 600 °C and 900 °C) and their resilience towards catalyst poisons at higher temperatures, including the possibility of catalyst regeneration via redox cycling.

A further outstanding ability of some perovskites is nanoparticle exsolution [25]. Upon reductive treatment (e.g. in H_2) or under reaction conditions (in sufficiently reducing reaction environments) the perovskite is partially reduced. Consequently, reducible lattice cations move to the surface, exsolve there, and form metallic nanoparticles. Catalytically highly active and easily reducible dopants are exsolved preferentially [21]. This process enables in-situ growth of active catalysts [23] and, in comparison to traditional deposition techniques, more finely and more highly dispersed catalyst nanoparticles are formed [25,26]. Moreover, this process is more economical (both with respect to time and cost), as no expensive precursors or complicated 'deposition' procedures are needed [27]. In addition, different studies have found that nanoparticles emerged via exsolution show enhanced sintering stability due to "anchoring", even at high reaction temperatures [25,28,29]. Hence, perovskites have the potential to resolve a major problem of many rWGS catalysts, i.e. rapid deactivation caused by severe aggregation of metal particles at high temperatures [13]. In fact, perosvkite catalysts are promising candidates to reduce similar problems in many CO_2 utilization reactions [30,31]. Moreover, Tsounis et al. could show that tailoring perovskites enables selectivity tuning and can also suppress competing side reactions [32].

Intensive research on nanoparticle exsolution and its mechanisms has been done already by the solid-state electrochemistry community [25,29,33]. Whether monometallic or bimetallic nanoparticles are formed during dopant and lattice cation reduction mainly depends on two factors: temperature and reductive power of the gas environment [34,35]. These properties open the possibility of catalyst engineering and tailoring materials for respective reactions.

The advantages outlined above were the motivation to synthesize not-yet intensively studied perovskite-based rWGS catalyst materials and to study their catalytic performance in the temperature range of 300 °C–700 °C and with different doping compositions including in situ XRD. The perovskite catalysts studied were $La_{0.9}Ca_{0.1}FeO_{3-\delta}$, $La_{0.6}Ca_{0.4}FeO_{3-\delta}$, $Nd_{0.9}Ca_{0.1}FeO_{3-\delta}$, $Nd_{0.6}Ca_{0.4}FeO_{3-\delta}$, $Nd_{0.6}Ca_{0.4}Fe_{0.9}Ni_{0.1}O_{3-\delta}$, and $Nd_{0.6}Ca_{0.4}Fe_{0.9}Co_{0.1}O_{3-\delta}$. The listed materials were selected due to current research on highly active rWGS materials and to demonstrate a possible design approach for finely tuned catalysts.

2. Experimental methods

2.1. Sample preparation

As described in previous work [21], the Pechini synthesis was used to prepare the samples. The following starting materials were mixed in the appropriate stoichiometric ratios: $La(CH_3COO)_3 \cdot 1.5H_2O$ (99.9 %, Alfa Aesar), Nd_2O_3 (99.9 %, Strategic Elements), $CaCO_3$ (99.95 %, Sigma-Aldrich), Fe (99.5 %, Sigma-Aldrich), $Co(NO_3)_3 \cdot 6H_2O$ (99.999 %, Sigma-Aldrich), and $Ni(NO_3)_3 \cdot 6H_2O$ (98 %, Alfa Aesar). Solutions (either in H_2O or in HNO_3 (65 %, Merck) – both doubly distilled) of the needed amounts were produced and mixed. A 20 % excess of citric acid (99.9998 % trace metal pure, Fluka) was added to the resulting mixtures to trigger complex formation. The solvents were evaporated off, self-ignition of the remaining gel was induced by heating, and the formed powders were calcined at 800 °C for 3 h. The Ni doped perovskite $Nd_{0.6}Ca_{0.4}Fe_{0.9}Ni_{0.1}O_{3-\delta}$ was additionally calcined a second time at 1000 °C, in order to try to achieve phase purity. The calcined products were homogenised via grinding and the powder samples were used for characterization [using Brunauer-Emmet-Teller (BET) analysis, scanning electron microscopy (SEM), and in-situ X-ray diffraction (XRD)] as well as catalytic experiments. Purchased $La_{0.6}Sr_{0.4}FeO_{3-\delta}$ (LSF, Sigma Aldrich) was catalytically tested with the same setup as a benchmark material. A Fe_2O_3/Cr_2O_3 WGS catalyst (HiFUEL™ W210, Thermo-Fischer Scientific) served as further reference. This commercially available catalyst can also serve as a tentative indicator of economic profitability: using the above-mentioned synthesis route and starting materials, production of the presented materials would cost about three times as much as the industrial catalyst. However, this is a very crude comparison, as no optimization or customization for industrial applications were done for the presented materials.

2.2. Structural and morphological characterization

A PANalytical X'Pert Pro diffractometer in Bragg–Brentano geometry (with separated Cu $K_{\alpha 1,2}$ radiation) and an X'Celerator linear detector was used to perform XRD measurements. The in-situ experiments

were carried out in an XRK 900 chamber (Anton Paar), providing a gas flow environment at ambient pressure. After a 30 min oxidative pre-treatment at 600 °C, the samples were cooled to room temperature and the reaction atmosphere of H_2 and CO_2 in a 1:1 ratio, using Ar as balancing gas, was switched on. Flows of 20 mL min^{-1} for each of the reaction gases and 50 mL min^{-1} of Ar were used for the experiments with $Nd_{0.6}Ca_{0.4}FeO_{3-\delta}$, while the respective flows were 7.5 mL min^{-1} and 15 mL min^{-1} for the experiments with $Nd_{0.6}Ca_{0.4}Fe_{0.9}Co_{0.1}O_{3-\delta}$ and LSF. The reaction was conducted at various temperatures and at each temperature step an in-situ XRD measurement was taken. To ensure equilibrium, each temperature was held for a period of 10 min prior to recording of the XRD pattern (~30 min per measurement), resulting in holding every temperature for about 40 min. Data analysis and reflex assignment were performed with the HighScore Plus software (PANalytical) and the PDF-4 + 2019 database (ICDD - International Centre for Diffraction Data) [36].

SEM images were recorded with secondary electrons on a Quanta 250 FEGSEM (FEI Company) microscope with an Octane Elite X-ray detector (EDAX Inc). An acceleration voltage of 5 kV was used for satisfactory surface-sensitivity.

2.3. Catalytic experiments

To assess the performance of the investigated samples, trial rWGS reactions were conducted in a tubular flow reactor at ambient pressure (the setup was already described in [37]). Continuous sampling of the gas atmosphere was carried out online (with a measurement every 2–3 min) using a Micro–Gas Chromatograph (Micro-GC, Fusion 3000A, Inficon). A carrier gas flow of 6 mL min^{-1} (Ar) was used, while for both reactive gases (CO_2 and H_2) a flow of 3 mL min^{-1} each was set, leading to an overall flow of 12 mL min^{-1} (the gases were purchased from Messer Group GmbH). To assess the effect of the reactor on the catalytic activity, a blank test without catalyst was conducted. The found value – which was ~0.5 Mol% for CO at 600 °C – was subtracted from all respective measurements for baseline correction of the measured conversion. The respective amounts of catalyst powder (20−75 mg) were chosen such, that the CO generation remained below the thermodynamic limit – which was tested by repeat measurements with reduced amounts. The chosen flow and catalyst masses resulted in Weight Hourly Space Velocities (WHSV) around 30 L g^{-1} h^{-1} (the exact values are given in Table 1 in Section 3.2). To make sure all test reactions start from the same state (fully oxidized perovskite), the samples were oxidized at 600 °C for 30 min in an oxygen atmosphere of 1 bar and a flow of 10 mL min^{-1} O_2.

Comparisons of catalytic performance reported in literature tend to be not straightforward: aside from a meaningful indicator regarding the performance, reaction conditions (temperature, pressure, composition of the reaction environment…) need to be given as well. Ref. [13], for instance, offers a nice overview of different catalysts used for rWGS for their given operating conditions. A common measure used by the catalytic community when comparing performances of catalysts are turn over frequencies (TOFs). However, in-depth knowledge about active sites (both nature and number) is necessary to feasibly obtain TOF values. This approach is hindered by the fact that perovskites are highly flexible (i.e. reaction parameter dependent) materials: For instance, the concentration of oxygen vacancies varies strongly depending on temperature. Moreover, the type of surface in contact with the reaction environment might vary (depending on dopants and termination). Also, possible (metal) nanoparticle exsolution influences the number of active sites, and consequently the activity, as well. Therefore, giving a TOF value is not straightforwardly possible. Instead, specific activities (activity per surface area) in mol m^{-2} s^{-1} were determined.

Table 1
BET surface areas, average specific activities calculated for CO production during rWGS at 600 °C and WHSVs of the respective measurements for all investigated perovskite materials.

Catalyst	BET area (m^2 g^{-1})	Specific Activity (10^{-6} mol m^{-2} s^{-1})	WHSV (L g^{-1} h^{-1})
$La_{0.9}Ca_{0.1}FeO_{3-\delta}$	3.8	5.7	24.6
$La_{0.6}Ca_{0.4}FeO_{3-\delta}$	2.8	5.9	34.1
$Nd_{0.9}Ca_{0.1}FeO_{3-\delta}$	2.2	11.3	32.7
$Nd_{0.6}Ca_{0.4}FeO_{3-\delta}$	1.5	6.6	20.5
$Nd_{0.6}Ca_{0.4}Fe_{0.9}Ni_{0.1}O_{3-\delta}$	1.6	18.0	36.0
$Nd_{0.6}Ca_{0.4}Fe_{0.9}Co_{0.1}O_{3-\delta}$	1.2	27.2	32.1
LSF	5.7	4.8	28.8

In order to calculate this specific activity, the specific surface areas a_S (in m^2 g^{-1}) of the materials (see Table 1 in Section 3.2.) were measured according to the BET method. Relevant isotherms of the degassed samples (4 h at 300 °C under vacuum) were obtained at −196 °C for fitting with a Micrometrics ASAP 2020 system. A specific activity r_{CO} in mol m^{-2} s^{-1} [measuring how many moles of product (CO) were formed per m^2 surface per s] was then derived according to Eq. (2), where the CO formation (mole fraction x_{CO} in the product stream) and the total gas flow $\dot{n}$ in mol s^{-1} were normalized to the catalyst surface area a_{CAT}. The total area a_{CAT} was obtained from the above-mentioned specific activity a_s and the used mass of catalyst m_{CAT}.

$$r_{CO} = \frac{\dot{n}\cdot x_{CO}}{a_{CAT}} = \frac{\dot{n}\cdot x_{CO}}{a_S \cdot m_{CAT}} \quad (2)$$

3. Results and discussion

3.1. Perovskite materials

Six different perovskite powders were manufactured for the current study. The investigated materials were chosen based on the following considerations:

(i) Ferrite type perovskites have been selected as starting point, since Fe has been proven to be catalytically active in rWGS reactions [18,38], and, therefore, provides an already active host lattice

(ii) Two of the investigated materials were B-site doped with 10 % Co or Ni, respectively. This means that in addition to an already catalytically active host lattice (see (i) above), further enhancements by reducible and catalytically active B-site dopants can be expected [4,39]. The reason for this expected enhancing effect of doping lies in the capability of the dopants of choice to – under the proper conditions (reductive atmosphere, high reaction temperatures) – diffuse to the surface and, by exsolution, form nanoparticles (as could be shown in previous studies [21,40]). Ni and Co are often used in combination with CeO_2 and/or Al_2O_3 as support materials for rWGS catalysts as e.g. shown by work of Wang et al. [39].

(iii) Nd and La were selected as A-cations, as both (as well as most rare earth elements) reportedly positively impact CO_2 utilization reactions in general [41]. Usually, the latter is a very wide-spread A-site element, however, additional materials with Nd instead of La were studied as well. This was done to evade potential problems arising from coinciding peaks of lattice elements and dopants (especially Ni) in future X-ray photoelectron spectroscopy (XPS) investigations.

(iv) Ca was used as A-site dopant in order to enhance electron and oxide ion conductivities (acceptor doping increases defect concentrations of electron holes and oxygen vacancies). A-site doping allows additional fine-tuning of the catalyst properties: both stability of the crystal as well as exsolution features can be affected [42]. For the doped perovskites here, 10 % and 40 % of Ca doping were chosen. Previous results [43] revealed effects of A-site dopant concentration on the electronic structure (more Ca leads to more partially oxidized Fe^{4+}) and an increase of perovskite stability, thus leading to higher exsolution onset temperatures. For the B-site doped materials enhanced lattice stability was found as well, leading to the assumption that mainly

dopants exsolve (given proper reducing conditions), while Fe ions remain in the lattice [21].

In short, the perovskite materials $La_{0.9}Ca_{0.1}FeO_{3-\delta}$, $La_{0.6}Ca_{0.4}FeO_{3-\delta}$, $Nd_{0.9}Ca_{0.1}FeO_{3-\delta}$, $Nd_{0.6}Ca_{0.4}FeO_{3-\delta}$, $Nd_{0.6}Ca_{0.4}Fe_{0.9}Ni_{0.1}O_{3-\delta}$, and $Nd_{0.6}Ca_{0.4}Fe_{0.9}Co_{0.1}O_{3-\delta}$, were selected for their content of catalytically active constituents, stability (both thermal and chemical), and exsolution capabilities. For additional comparison, commercial $La_{0.6}Sr_{0.4}FeO_{3-\delta}$ (LSF, Sigma Aldrich) was used as reference. Characterization of the produced powders (structure and exsolution capabilities) was performed with XRD and SEM (details have been published in [43]). The XRD measurements revealed that all materials could be prepared successfully and that for all perovskites but the Ni-doped only the perovskite phase was present. They have similar distorted perovskite structures with an orthorhombic lattice, consistent with reports for $La_{(1-x)}Ca_xFeO_3$ perovskites [44]. In case of $Nd_{0.6}Ca_{0.4}Fe_{0.9}Ni_{0.1}O_{3-\delta}$, minimal amounts of NiO were found (cf. Fig. S2), meaning that Ni was not fully integrated. No additional phases were found for the Co-doped material, indicating complete incorporation. The commercial LSF is, due to the larger Sr cations compared to Ca, differently distorted with a rhombohedral lattice.

To obtain the surface area of all synthesized catalyst materials, BET analyses carried out on the freshly prepared powders yielded surface areas ranging from 1.13 $m^2\ g^{-1}$ to 5.07 $m^2\ g^{-1}$ (see Table 1 in Section 3.2).

3.2. rWGS shift activity and selectivity

To ensure the same starting conditions in all experiments and comparability of the results, all samples were pre-treated oxidatively (30 min in pure O_2 at 600 °C). In a second preparation step, the temperature of samples was reduced to 300 °C, and only then, the gas atmosphere was changed to the reaction mixture. For all experiments the CO_2 and H_2 ratio was set to 1:1. Care was taken with respect to the used mass of catalyst, so that the reaction proceeds away from thermodynamic equilibrium (i.e. at 600 °C and 700 °C the limit is 40 % and 45 %, respectively). This has to be taken into account, since conversion rates around the equilibrium lead to pronounced back reaction contributions (WGS instead of rWGS) [45]. After switching to the reaction mixture, 60-minutes measurements were conducted between 300 °C and 700 °C. The temperature was increased in 100 °C steps.

Fig. 1 exemplarily displays the results for rWGS on the B-site undoped perovskite $La_{0.6}Ca_{0.4}FeO_{3-\delta}$. Switching on the reaction environment at low temperatures (300 °C) did not lead to detectable activity. Only after the reaction temperature was raised to 400 °C, the onset of CO formation was observed. Similar onset temperatures where noted by Daza et al. on a related perovskite ($LaFeO_3$) with a CO formation onset temperature of 450 °C and similarly high CO selectivity [16]. When raising the reaction temperature to 500 °C and 600 °C, the CO formation increased significantly (~15 % conversion at 600 °C). It is worth mentioning that parallel consumption of the educts CO_2 and H_2 is also nicely visible in Fig. 1. This is especially important to note, since the amount of formed water could unfortunately not be quantified with desired accuracy by the used Micro-GC, despite water being visible in the chromatogram. All comparisons presented in this study use the reactivity values found at 600 °C, since educt conversion at 700 °C is too close to the thermodynamic equilibrium.

The same procedure was used to assess the rWGS performance of all synthesized perovskites as well as of commercial LSF. In Fig. 2 a comparative summary of all results is shown. Area specific activities (in mol m^{-2} s^{-1}) were used for direct comparisons of the CO formation rate. To get the necessary values for such a comparison, the catalytic activity was related to the active surface areas, see Section 2.3 for details. In Table 1, all average specific activities at 600 °C are given.

The lowest activities were found for the La-based B-site undoped samples ($La_{0.9}Ca_{0.1}FeO_{3-\delta}$and $La_{0.6}Ca_{0.4}FeO_{3-\delta}$, purple curves in Fig. 2), which are comparable to the results of LSF (Fig. 2, black curve). Increasing the A-site dopant concentration had only a minor effect on the activity. The specific activity at 600 °C was 5.7 × 10^{-6} mol m^{-2} s^{-1} and 5.9 × 10^{-6} mol m^{-2} s^{-1}, respectively (for LSF it was 4.8 × 10^{-6} mol m^{-2} s^{-1}). A change of A-site dopant (going from La to Nd) increased the activity ($Nd_{0.9}Ca_{0.1}FeO_{3-\delta}$ and $Nd_{0.6}Ca_{0.4}FeO_{3-\delta}$, orange curves in Fig. 2). Both materials showed a CO formation onset when raising the temperature to 400 °C. With every temperature step a further increase of activity was observable. The material with the lower Ca-doping (10 %) exhibited higher CO formation rates than the perovskite with higher Ca content at 600 °C and 700 °C. The specific activities at 600 °C were 11.3 × 10^{-6} mol m^{-2} s^{-1} and 6.6 × 10^{-6} mol m^{-2} s^{-1} for $Nd_{0.9}Ca_{0.1}FeO_{3-\delta}$ and $Nd_{0.6}Ca_{0.4}FeO_{3-\delta}$, respectively.

A comparison of activities found for the Ni-doped sample $Nd_{0.6}Ca_{0.4}Fe_{0.9}Ni_{0.1}O_{3-\delta}$ in Fig. 2 (blue curve) and the undoped $Nd_{0.6}Ca_{0.4}FeO_{3-\delta}$ indicates that doping positively affects CO formation at elevated temperatures. Furthermore, it could be observed that at 500 °C CO formation increased initially (unlike for the undoped materials, where the activity during each step was either constant or showed an initial drop). At 600 °C, the specific activity for the Ni doped perovskite was 18.0 × 10^{-6} mol m^{-2} s^{-1}. The material doped with Co exhibited similar activation phenomena (Fig. 2, green curve). Already at 400 °C, a

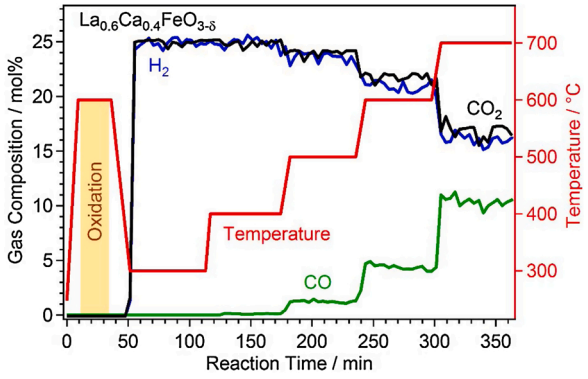

Fig. 1. Gas composition of rWGS reaction on $La_{0.6}Ca_{0.4}FeO_{3-\delta}$. The temperature programme (300 °C to 700 °C) was started after 30 min at 600 °C in pure O_2. Contents of CO (green), CO_2 (black), and H_2 (blue) are shown (please note that 50 % of the feed gas was Ar). CO formation started at 400 °C. (For interpretation of the references to colour in this figure legend, the reader is referred to the web version of this article.)

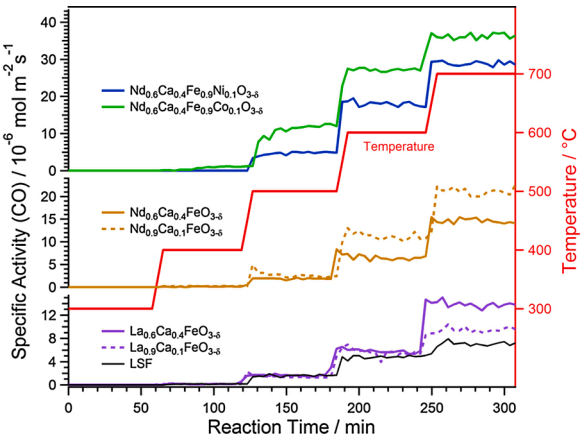

Fig. 2. Comparison of rWGS results. The reaction rates of CO formation are displayed as surface specific activities in mol m^{-2} s^{-1} (note the different scales). LSF is included as benchmark (black line). For the reactions a 1:1 gas mixture of H_2 and CO_2 was used, and the temperature was increased in steps of 100 °C from 300 °C to 700 °C. For all temperatures, Co- and Ni-doped samples exhibited the best activities.

slight increase of the CO formation could be observed in the isothermal regime. At 500 °C, this effect was even stronger. When comparing all activities at all used temperatures, the largest value (27.2×10^{-6} mol m^{-2} s^{-1} at 600 °C) was found for the Co-doped perovskite.

Besides comparing the novel perovskites to LSF, benchmarks of the catalytic performance against an industrial catalyst were conducted as well. Hence, the rWGS reaction was performed with the same parameters on the commercial HiFuel™ high temperature WGS catalyst. It is composed primary of iron oxide with 7 % chromium oxide to enhance sinter stability, which makes the catalyst ideal for comparison to the iron-based perovskites of this study. At 600 °C, the obtained specific activity was $\sim 3 \times 10^{-7}$ mol m^{-2} s^{-1}, which is one order of magnitude lower than for the investigated undoped perovskites. But this result has to be evaluated very critically, as very strong sintering and consequently reduction of active surface area of the commercial catalyst was observed at high reaction temperatures. Consequently, the comparability of the specific activity of this reference material is questionable.

To summarize, we found that exchanging La with Nd increases the catalytic activity, and doping the perovskite B-site with Ni or Co enhanced it even further. The Co-doped catalyst exhibited the best performance, highlighting that Co-doping is highly beneficial to rWGS activity. The activity enhancing effects of the addition of Co were reported for other materials, e.g. metal-carbides, as well [46].

There are two conceivable reasons for the high activities observed in the Ni- and Co-doped perovskites: (i) exsolution of nanoparticles (which is a well-documented phenomenon in perovskites [25]) and (ii) reducibility of the materials.

In literature and in previous work done by the authors, it was shown that nanoparticle exsolution can greatly enhance the catalytic activity of perovskites [34,47]. Moreover, the ongoing process of nanoparticle formation could be an explanation for the increasing activity over time at constant temperature observed for the Ni (500 °C) and Co (400 °C and 500 °C) doped catalysts. Exsolution and the observed structural and morphological changes of our catalysts will be treated in depth in Section 3.3.

With respect to reducibility, it should be noted that compared to the undoped perovskites, $Nd_{0.6}Ca_{0.4}Fe_{0.9}Ni_{0.1}O_{3-\delta}$ and $Nd_{0.6}Ca_{0.4}Fe_{0.9}Co_{0.1}O_{3-\delta}$ are more easily reduced in the reaction environment, as was demonstrated in a chemical looping experiment for Co-doping (see supporting info, Fig. S1). Furthermore, it has been shown by various groups that the rWGS reaction of catalysts containing an easily reducible oxide (e.g. as support) follows a surface redox mechanism (see for example the Pt/ceria or iron oxide based systems in Refs. [48,49]).

Both aspects will be discussed more thoroughly in Section 3.5., giving a more detailed mechanistic insight.

In addition, the occurrence of any side reactions was checked for all tested materials. Methane, for example, is a very well know side product, as the Sabatier reactions are the main side reactions of rWGS [4]. Here, however, no side products could be detected in the gas chromatograms indicating a high CO-selectivity: A key factor for a high selectivity towards CO – and an important property of perovskites – is the reducibility of the oxide support material, the oxygen ion mobility, and its capability for vacancy formation. For instance, for rWGS on the perovskites $BaZr_{0.8}Y_{0.16}Zn_{0.04}O_3$ and $La_{0.75}Sr_{0.25}FeO_3$ nearly 100 % CO selectivity have been reported [4,15]. Also, O vacancies have been reported to be crucial for the catalytic activity of the $Pd/CeO_2/Al_2O_3$ system, as they can be filled with O from CO_2 [50]. One possible further reason for the high selectivity of the tested systems could be the size and distribution of the exsolved nanoparticles as discussed below. Similarly, Lu et al. observed that low Ni loadings (< 3 %) with well dispersed nanoparticles are highly beneficial to the selectivity towards CO [51]. They reported 100 % CO selectivity in the temperature range from 400 °C to 750 °C.

3.3. Exsolution properties investigated by (in-situ) XRD and SEM

To directly follow the structural changes of the novel perovskites during catalytic reactions and to get insights into the active phase of the different perovskites, in-situ XRD measurements were performed in the reaction environment (i.e. at 1 bar in a flow cell, 1:1 ratio of CO_2 and H_2) on selected perovskites. Resulting XRD diffractograms for the undoped $Nd_{0.6}Ca_{0.4}FeO_{3-\delta}$ are shown in Fig. 3.

At low rWGS reaction temperatures (below 400 °C), only the reflexes corresponding to the perovskite host lattice were visible. Importantly, the perovskite was stable and no decomposition of the material was observed at all reaction temperatures. This is crucial for possible industrial applications, where catalyst regeneration by oxidation/reduction cycles can be realized on stable materials [52]. Although rWGS reaction conditions are reducing, no formation of any metallic Fe-phase could be observed by in-situ XRD over the whole temperature range of the experiment. The chemical potential of the gas phase was not sufficient for the formation of metallic nanoparticles on the surface. However, between 500 °C and 600 °C weak signals (2θ of 30.0°, 35.3° and 62.0°) were evolving, which could be assigned to the occurrence of Fe_3O_4. This phase transformed to FeO at around 600 °C, indicated by the disappearance of the Fe_3O_4 signals and emerging signals at 2θ of 36.0°, 41.8°, and 60.5°. This transition agrees with the Fe-O phase diagram [53], which shows a transition around 570 °C. It was previously reported that iron-oxide is an active phase for catalysing rWGS [4], and in the current experiments this phase is forming under reaction conditions.

Additionally, at a temperature of 400 °C a small signal evolved at 2θ of 29.4°, resulting from formation of $CaCO_3$ on the perovskite surface. Similarly, above 500 °C trace amounts of a graphite phase could be observed. Formation of carbonates under reaction conditions is a well-known phenomenon for A-site doped perovskites, as reported in literature [54]. The amount of $CaCO_3$ increased at higher reaction temperatures, simultaneously with the formation of the iron oxide species. This might be due to the additional driving force of establishing stoichiometric balance in the perovskite structure after the exsolution of B-site cations. Interestingly, both iron-oxide and $CaCO_3$ signals diminish at the highest temperature of 700 °C.

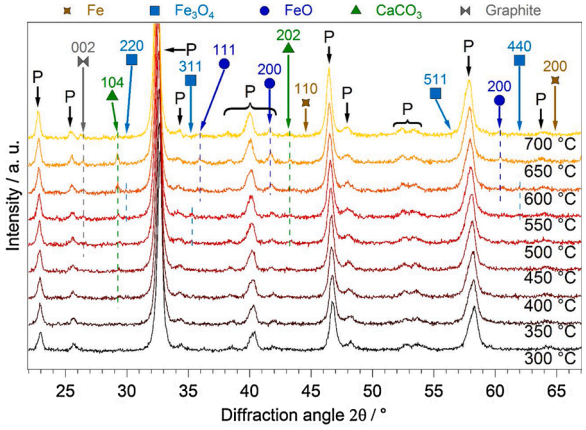

Fig. 3. In-situ XRD results during the rWGS reaction on $Nd_{0.6}Ca_{0.4}FeO_{3-\delta}$ displayed in the temperature range of 300 °C to 700 °C. Signals corresponding to the perovskite host lattice are marked with "P". No formation of metallic Fe was observed in the investigated temperature range. Between 500 °C and 600 °C, small amounts of Fe_3O_4 were found. Above 600 °C, these signals disappeared, while at the same time an FeO phase emerged (signals at 2θ of 36.0°, 41.8°, and 60.5°). Already at 400 °C, a small signal evolved at 2θ of 29.4° as well as a result of $CaCO_3$ formation on the perovskite surface. This signal increased at higher temperatures, simultaneously with the iron oxide formation. In addition, trace amounts of graphite could be observed above 500 °C.

Figs. S3–S6 in the supporting info show diffractograms of all the B-site undoped samples, $La_{0.9}Ca_{0.1}FeO_{3-\delta}$, $La_{0.6}Ca_{0.4}FeO_{3-\delta}$, $Nd_{0.9}Ca_{0.1}FeO_{3-\delta}$, and $Nd_{0.6}Ca_{0.4}FeO_{3-\delta}$, obtained by ex-situ XRD after rWGS reactions (samples from the activity measurements with the last temperature at 700 °C). In agreement with the in-situ XRD results, for $Nd_{0.6}Ca_{0.4}FeO_{3-\delta}$ both $CaCO_3$ and an iron-oxide phase were found. The latter is Fe_3O_4, probably because FeO present at the highest temperatures (see in-situ XRD experiment) underwent a phase transition back to Fe_3O_4 when cooling down.

For $Nd_{0.9}Ca_{0.1}FeO_{3-\delta}$, Fe_3O_4 was also visible, as well as trace amounts of $CaCO_3$. In contrast, for the samples with La no iron-oxide species could be observed. Furthermore, for $La_{0.9}Ca_{0.1}FeO_{3-\delta}$ no new phases were found at all after rWGS, while for $La_{0.6}Ca_{0.4}FeO_{3-\delta}$ formation of $CaCO_3$ was observed. Two trends follow from these observations. Firstly, the exchange of La with Nd enables the formation of the iron oxide phases under rWGS conditions. Secondly, more Ca-doping on the perovskite A-site leads to stronger $CaCO_3$ formation during reaction, as would be expected.

Another observation arising when comparing the diffractograms before and after rWGS is the slight shift of all reflex positions towards smaller diffraction angles. This effect is strongest for $La_{0.6}Ca_{0.4}FeO_{3-\delta}$ and is due to expansion of the unit cell in reducing conditions as the result of oxygen vacancies being formed and the partial reduction of the Fe (from Fe^{4+} to Fe^{3+} and from Fe^{3+} to Fe^{2+}) [55].

Formation of $CaCO_3$ was also visible in SEM images recorded after rWGS reactions on $La_{0.6}Ca_{0.4}FeO_{3-\delta}$ and $Nd_{0.6}Ca_{0.4}FeO_{3-\delta}$, Figs. S8/S10. After reaction, larger crystals with regular shape (often triangular) and sizes between 200 nm and 400 nm could be observed. These crystals were assigned to $CaCO_3$ (this was supported by EDX measurements performed on the B-site doped materials, see below). In case of lower Ca-doping, $La_{0.9}Ca_{0.1}FeO_{3-\delta}$ and $Nd_{0.9}Ca_{0.1}FeO_{3-\delta}$, no $CaCO_3$ can be seen in the SEM images (Figs. S9/S11). For B-site undoped materials, no formation of nanoparticles was observed on the perovskite surface by SEM, although formation of FeO could be observed for $Nd_{0.6}Ca_{0.4}FeO_{3-\delta}$ by in-situ XRD and Fe_3O_4 could be found for both perovskites with Nd in the ex-situ XRD patterns. Conceivably, iron oxide occurred either as exsolved nanoparticles that were below the detection limit of SEM, or decomposition occurred without apparent changes in morphology. Generally, the perovskites preserved their overall surface structure (except for $CaCO_3$ formation), highlighting their excellent thermal stability.

The absence of metallic surface iron species on the B-site undoped $Nd_{0.6}Ca_{0.4}FeO_{3-\delta}$ could also be confirmed by in situ NAP-XPS data (cf. Fig. S14A).

In-situ XRD measurements on the reference material LSF (Fig. S7) showed a very similar behaviour as for $Nd_{0.6}Ca_{0.4}FeO_{3-\delta}$. At low reaction temperatures, only the perovskite phase was observable. At 650 °C, the formation of FeO could be observed, as indicated by the weak signal at 2θ of 41.7°. Moreover, trace amounts of $SrCO_3$ started to appear at 2θ of 25.0°, analogous to the formation of $CaCO_3$ in the Ca doped materials. Unlike for the Ca doped samples, SEM could reveal the formation of small nanoparticles (20−30 nm) on the perovskite surface for LSF, Fig. S12.

To investigate the influence of exsolution on the rWGS activity, the experiment on $Nd_{0.6}Ca_{0.4}FeO_{3-\delta}$ was repeated with an additional pre-treatment step in H_2/H_2O (32:1) at 700 °C (60 min). The bottom XRD pattern in Fig. 4 indicates successful Fe nanoparticle formation by reductive treatment (2θ of 44.6° and 62.9°, corresponding to a metallic Fe-phase), which has already been shown in earlier work [21].

Upon stepwise increases of the rWGS reaction temperature, the metallic Fe signal started to decrease between 450 °C and 500 °C. At the same time, new diffraction lines appeared at 2θ of 30.0°, 35.3°, 56.6°, and 62.2°, which could be assigned to Fe_3O_4. Under rWGS reaction conditions, the initially metallic Fe nanoparticles where oxidized to Fe_3O_4 in the temperature range of 450 °C–550 °C. Between 600 °C–650 °C, a further change of the observed phases occurred. The

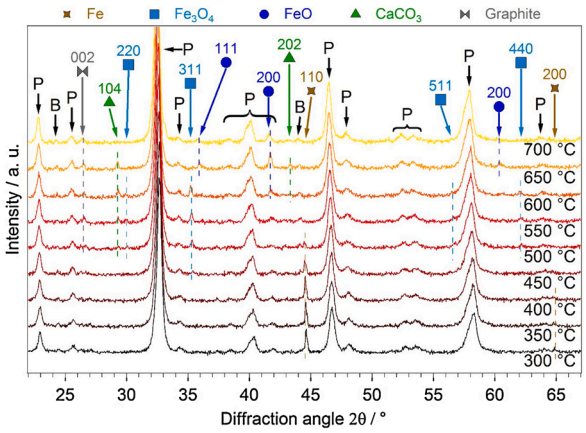

Fig. 4. Repeated in-situ XRD measurement for $Nd_{0.6}Ca_{0.4}FeO_{3-\delta}$, displayed from 300 °C to 700 °C. Signals corresponding to the perovskite host lattice are marked with "P". For this experiment the perovskite was reduced in H_2/H_2O prior to the catalytic reaction at 700 °C for 60 min. Pre-treatment resulted in the exsolution of metallic Fe nanoparticles, evidenced by reflexes at a 2θ of 44.6° and 62.9°. With increasing reaction temperature, the metallic Fe vanished completely above 550 °C. At the same time, the appearance of Fe_3O_4 signals at 2θ of 30.0°, 35.3°, 56.6°, and 62.2° was visible, resulting from the transformation of metallic Fe to Fe_3O_4 under rWGS conditions. Above 550 °C, weak reflexes at 2θ of 35.9°, 41.7°, and 60.4° were evolving, which correspond to FeO. At reaction temperatures above 500 °C, a small signal was observed at 2θ of 29.3°, corresponding to formation of $CaCO_3$ on the perovskite surface.

Fe_3O_4 nanoparticles where reduced to FeO (2θ of 35.9°, 41.7°, and 60.4°). Additionally, starting from 500 °C, $CaCO_3$ and graphite were formed. At the highest reaction temperature (700 °C), the carbonate phase diminished and only FeO and graphite were left on the catalyst surface.

In combination with the activity data of the catalytic measurements (cf. Section 3.2), it can be concluded that the formed Fe_3O_4 and FeO is correlated to the high rWGS activity. While the specific activities of all the B-site undoped materials were similar at 500 °C, starting from 600 °C, the Nd-based perovskites exhibited higher catalytic activities compared to the respective perovskites with La. The temperature region between 500 °C and 600 °C is exactly where the iron-oxide phases started to evolve in the in-situ XRD experiment with $Nd_{0.6}Ca_{0.4}FeO_{3-\delta}$. Furthermore, an iron-oxide phase only occurred in the ex-situ XRD experiments with the Nd-based perovskites. This phase is formed under reaction conditions, both from the perovskite without reductive pre-treatment and from already exsolved Fe particles. The unwanted formation of $CaCO_3$ observed for the materials with a higher amount of Ca-doping could explain why the activity of $Nd_{0.6}Ca_{0.4}FeO_{3-\delta}$ was lower compared to $Nd_{0.9}Ca_{0.1}FeO_{3-\delta}$. These results demonstrate how rich the surface chemistry of perovskites can be, and that the surface is responding dynamically to changes of the chemical potential of the reaction environment, as well as the strong effect these changes have on the rWGS activity.

In-situ XRD results for the Co-doped perovskite $Nd_{0.6}Ca_{0.4}Fe_{0.9-x}Co_{0.1}O_{3-\delta}$ are displayed in Fig. 5. Here, the catalyst was exposed to the rWGS reaction environment without any reductive pre-treatment (only initial oxidation was performed for a defined surface state). Above 525 °C, the formation of a FeO and/or CoO phase could be observed at 2θ of 36.2°, 40.0°, and 60.7°. Unfortunately, it was not possible to find a clear assignment to either FeO or CoO (or a mixed Fe-Co-oxide – $Fe_xCo_{1-x}O$) due to the overlap of the two signals in XRD and the limited resolution of the diffractometer. However, from previous work with EDX mapping, it is known that due to easy reducibility Co is preferentially exsolved at lower temperatures [21]. At 550 °C, additional formation of a metallic bcc phase could be observed at 2θ of 44.8° and 65.0°. Again, no clear assignment was possible with XRD due to the signal overlap of

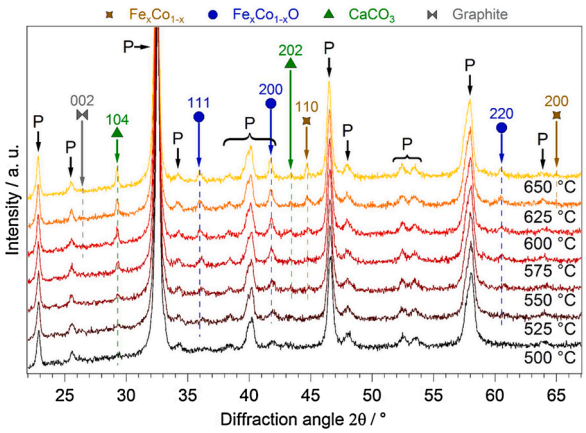

Fig. 5. In-situ XRD results during the rWGS reaction on cobalt doped $Nd_{0.6}Ca_{0.4}Fe_{0.9}Co_{0.1}O_{3-\delta}$, displayed in the temperature range of 500 °C to 650 °C. Signals corresponding to the perovskite host lattice are marked with "P". Above 550 °C, a signal starts to evolve at a 2θ of 44.8° associated with either a Fe or a Co bcc phase. In the same temperature range, signals at 2θ of 36.2°, 40.0°, and 60.7° can be observed, which could be attributed to either CoO or FeO. Starting from the lowest temperature at 2θ of 29.3°, an increasing amount of formed $CaCO_3$ was found.

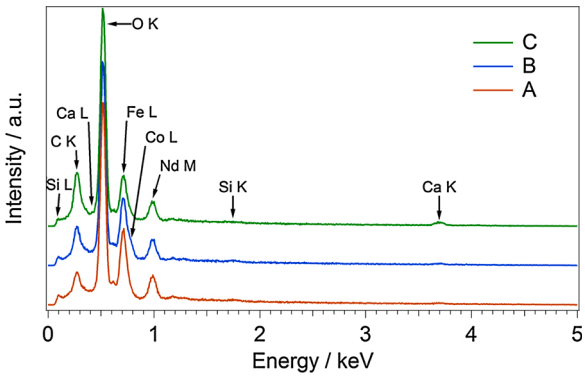

Fig. 7. EDX spectra obtained at the indicated spots A, B and C in Fig. 6 on $Nd_{0.6}Ca_{0.4}Fe_{0.9}Co_{0.1}O_{3-\delta}$ after rWGS reaction. Spectrum A corresponds to the perovskite surface; spectrum B to a formed nanoparticle, where an enrichment of Co was detected; and spectrum C was taken at the position of a larger crystallite that could be identified to consist of $CaCO_3$ due to enrichment in Ca and C.

Fe and Co, however the fact that no metallic phase occurred in the experiment without Co-doping (cf. Fig. 3), the higher diffraction angle compared to the metallic phase in the experiment with B-site undoped $Nd_{0.6}Ca_{0.4}FeO_{3-\delta}$ and pre-treatment (cf. Fig. 4), and the preferential exsolution of Co suggest a predominance of Co in this phase. Both the B-site metal oxide and metallic phases are more pronounced than in the case of no Co doping. These results show that doping with Co enhances the exsolution process and also enables the reduction of the exsolved elements to a metallic state within the reaction atmosphere, which is preferred for catalysis. These findings where supported by in situ NAP-XPS data as well (cf. Fig. S14B), with the evolvement of metallic Co during rWGS reaction. Already at 500 °C, a small amount of $CaCO_3$ could be observed at 2θ of 29.3°, which got larger simultaneously with the formation of the B-site cation containing phases. Importantly, the perovskite host lattice was stable over the whole temperature range.

Figs. 6 and 7 summarize the results from SEM and EDX measurements for $Nd_{0.6}Ca_{0.4}Fe_{0.9}Co_{0.1}O_{3-\delta}$. After the rWGS reaction, larger, smooth crystals (sizes around 250 nm) on the surface could be observed. They could be identified as formed $CaCO_3$ on the surface, which was supported by the enrichment of Ca and C seen in the EDX spectrum at the position of one of these crystallites (Fig. 7, spectrum C). Furthermore, the formation of finely dispersed nanoparticles with sizes between 20 nm and 50 nm was visible. The EDX spectrum at the position of one particle (Fig. 7, spectrum B) reveals a larger Co L signal (as a shoulder of the Fe L peak) compared to a position in between particles (Fig. 7, spectrum A). This supports the theory that Co has been preferentially exsolved before Fe, and that the nanoparticles can be supposed to be mainly composed of Co. It should be pointed out that the spatial and depth resolution of the EDX analysis is limited, meaning that the obtained spectrum includes signals from the surrounding of the particle. Therefore, an unequivocal determination of the particle composition would require additional TEM studies.

The in-situ XRD results suggest that during reaction the nanoparticles were either primarily metallic or already oxidized. Due to the exposure to air (and hence oxidation), when transferring the samples to the SEM, it is no longer possible to distinguish between the two cases. Therefore, it is not clear which of the B-site metal oxide or metallic phases observed with XRD, or even both, correspond to the nanoparticles seen in the SEM images. Astonishingly, these nanoparticles were stable without sintering effects even at high reaction temperatures up to 700 °C. The reason is that nanoparticles formed by exsolution are anchored to the perovskite surface, as has been shown by Neagu et al. [33] in an in-situ TEM study. The stable nature and the prevention of sintering of these formed nanoparticles make perovskite catalysts extremely valuable for industrial applications.

As shown in the catalytic data (cf. Section 3.2), the Co-doped perovskite exhibited the highest rWGS activity. A possible reason could be the co-existence of nanoparticles containing metallic Co and the FeO/CoO oxide phase on the perovskite surface (in vicinity to oxygen vacancies of the host lattice), both enhancing hydrogen dissociation and redox activity (further details see Sec. 3.5 below). This is supported by the fact that the activity measurements of the Co-doped catalyst showed the largest increase between 500 °C and 600 °C, the temperature region where these phases started to appear in the in-situ XRD

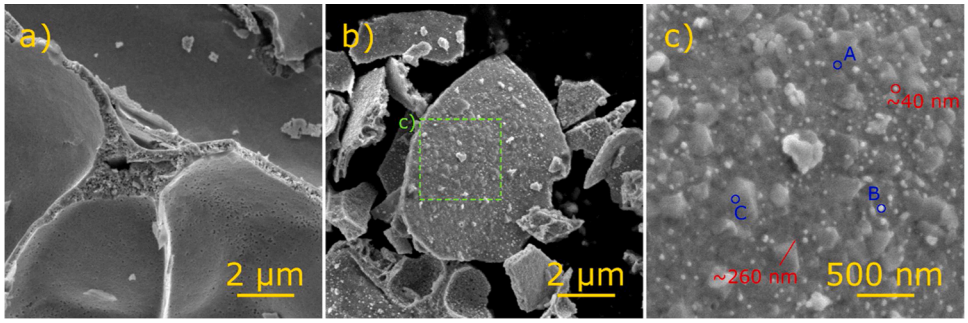

Fig. 6. SEM Images of $Nd_{0.6}Ca_{0.4}Fe_{0.9}Co_{0.1}O_{3-\delta}$ after a) calcination at 800 °C (pristine state) and b) after the rWGS reaction at 700 °C; c) is a section (green dashed box) shown at higher magnification. The bright flakes on the surface in a) and b) are small pieces left from the grinding following the synthesis. After the rWGS reaction, bigger, smooth crystals on the surface with sizes of around 250 nm could be observed. They could be assigned to $CaCO_3$ that was formed during reaction. Furthermore, finely distributed nanoparticles with sizes around 40 nm are present in c) that were exsolved under reaction conditions. Positions A, B and C indicate the spots where EDX spectra were obtained (see Fig. 7). (For interpretation of the references to colour in this figure legend, the reader is referred to the web version of this article.)

experiment. For Sr-doped lanthanum cobaltite perovskites ($La_{1-x}Sr_xCoO_{3-\delta}$), Daza et al. reported the importance of metallic cobalt for the conversion of CO_2 to CO as well [56].

For the Ni doped catalyst $Nd_{0.6}Ca_{0.4}Fe_{0.9}Ni_{0.1}O_{3-\delta}$, a diffractogram was obtained ex-situ after rWGS reaction (Fig. S2 in the supporting information) using the sample from the activity measurement (last temperature 700 °C). Here, the NiO impurity observed in the pristine sample could not be found anymore. Instead, a metallic Ni-phase (fcc) was present, indicated by the reflexes at 2θ of 43.9° and 51.2°. This suggests a reduction of the NiO phase to metallic Ni during rWGS, probably around 500 °C, which is the temperature where increasing activity at constant parameters was observed in the catalytic experiments. The formation of additional metallic Ni (by exsolution) cannot be confirmed conclusively. Also, alloying of Ni with Fe within the fcc phase might be possible by exsolution. Further experiments would be necessary to determine the exact behaviour. Besides the Ni containing phases, formation of $CaCO_3$, as well as trace amounts of Fe_3O_4 could be observed. This agrees with the results observed for the B-site undoped $Nd_{0.6}Ca_{0.4}FeO_{3-\delta}$. Compared to the latter, there was more $CaCO_3$ and less Fe_3O_4. This can be explained by the changed driving forces for segregation, evoked by the formation of the Ni phase. As this leads to a B-site sub-stoichiometry in the remaining perovskite, the A-site Ca segregation is enhanced, while B-site Fe segregation is reduced.

The larger $CaCO_3$ crystals found on the surface of $La_{0.6}Ca_{0.4}FeO_{3-\delta}$, $Nd_{0.6}Ca_{0.4}FeO_{3-\delta}$, and $Nd_{0.6}Ca_{0.4}Fe_{0.9}Co_{0.1}O_{3-\delta}$ were also observed in the SEM images of $Nd_{0.6}Ca_{0.4}Fe_{0.9}Ni_{0.1}O_{3-\delta}$ (Fig. S13). Here, they were even bigger with sizes between 400 nm and 700 nm. This larger size matches the result of an enhanced Ca segregation obtained from the XRD measurements. Furthermore, the larger size of the crystals allowed for an EDX mapping to confirm their chemical nature as $CaCO_3$. At high magnification, also very small nanoparticles (< 15 nm) were visible on the surface. These probably consist of Ni, in agreement with the metallic Ni-phase observed with XRD. The formation of Ni nanoparticles can explain the higher catalytic activity of the Ni-doped catalyst compared to the undoped ones, which was observed in the catalytic measurements (cf. Section 3.2).

3.4. Enhancement of rWGS activity by exsolution

To further investigate the promoting effect of the formed nanoparticles, and to answer if the exsolved nanoparticles are really enhancing the catalytic activity, additional experiments were conducted. These additional activity tests for $Nd_{0.9}Ca_{0.1}FeO_{3-\delta}$ and $Nd_{0.6}Ca_{0.4}Fe_{0.9}Co_{0.1}O_{3-\delta}$ were performed with linear temperature ramps.

For the undoped $Nd_{0.9}Ca_{0.1}FeO_{3-\delta}$, it was found that exsolution of metallic Fe particles does not enhance the catalytic activity (for more details see the supporting info Section "Exsolution Enhanced Catalytic Reaction" and Fig. S15).

For the B-doped $Nd_{0.6}Ca_{0.4}Fe_{0.9}Co_{0.1}O_{3-\delta}$, the reaction temperature was increased from 300 °C to 570 °C (heating rate =1 °C min^{-1}). After reaching 570 °C, the reaction temperature was reduced with the same rate (to 300 °C) (see also Fig. S16). For this special experiment 570 °C was chosen as highest temperature, because at this temperature exsolution is already possible, but $CaCO_3$ formation is still minor (see in-situ XRD results, Fig. 5). From the in-situ XRD results, in this temperature range the exsolved particles are expected to be mainly cobalt-oxide.

Since the cobalt-oxide-nanoparticles only form upon the first heating in reaction atmosphere (they are formed in-situ at high reaction temperatures where cation mobility is sufficient), heat-up and cool-down behaviour are expected to be different in case the particles affect the activity of the catalyst. If the formed nanoparticles would have no influence on catalytic reactivity, the CO formation rate should be equal for both up and down ramping. Indeed, a hysteresis-like behaviour was found as can be seen in Fig. 8, with a maximum increase in formed CO by 0.9 mol% at 490 °C. This is a clear indication that for the cooling ramp a higher catalytic reactivity was observed than for the heating ramp,

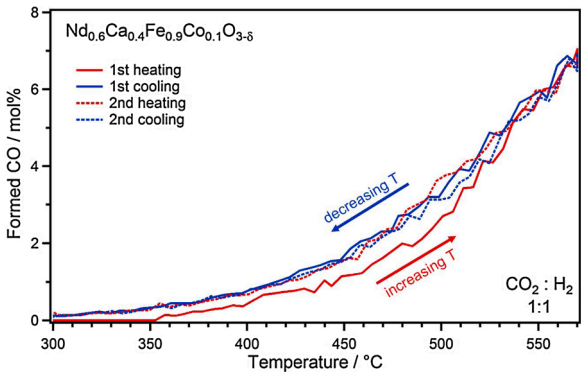

Fig. 8. CO formation during rWGS reaction on $Nd_{0.6}Ca_{0.4}Fe_{0.9}Co_{0.1}O_{3-\delta}$. The reaction temperature was increased with a linear ramp of 1 °C per minute to 570 °C and then reduced to 300 °C with the same rate (full curves). During the initial ramp, nanoparticles were formed on the surface, which were improving the rWGS activity. While cooling, a hysteresis with increased reactivity is visible, caused by the formed nanoparticles. When repeating the experiment on the used catalyst (dashed curves), the same higher activity was observed, as the exsolved nanoparticles were present during the heating ramp as well.

which can be interpreted as an evidence for a catalytic effect of the exsolved nanoparticles.

To show that this method is genuinely suitable of determining differences in catalytic activity, a second identical experiment was conducted directly after the first heat-up/cool-down cycle (i.e. without changing the catalyst, and without any intermediate treatment). The catalytic activity during both the second heating and cooling phases followed the cooling ramp of the first cycle exactly (see Fig. 8, dashed curves). This confirms that nanoparticles, evolving upon the very first heat-up, were improving the rWGS reactivity over the whole temperature range of all following heat-up or cool-down ramps, indicating reversible and stable catalytic behaviour of the nanoparticle decorated perovskite catalyst. Consequently, with this experiment strong structural deactivation phenomena in the investigated temperature range (up to 570 °C, prior to the increased formation of $CaCO_3$) could be ruled out as well.

3.5. Mechanistic relation between surface structure and catalytic activity

In heterogeneous catalysis on reducible oxides, commonly lattice oxygen is found in the reaction product. This effect was explained by P. Mars and D. W. van Krevelen by suggesting a regenerative redox mechanism that consists of two steps [57]: In the first step, the catalyst is reduced by one of the educts, which is oxidized by taking up an oxygen atom from the catalyst and thus creates a vacancy in the catalyst's oxygen sub-lattice. In the following second step, the catalyst is regenerated by reaction with the second educt, which donates an oxygen atom to the catalyst and hence becomes reduced.

The rWGS reaction (Eq. (1)) on oxide catalysts usually also proceeds *via* a Mars-van Krevelen (MvK)-type redox mechanism. There, in the first step, hydrogen reacts with lattice oxygen of the catalyst forming the first product water, which desorbs leaving an oxygen vacancy behind. The two electrons formed in this reaction step are also transferred to the catalyst oxide ensuring charge neutrality. In Eq. (3) the half reaction of H_2 oxidation proceeding on a reducible oxide is written in Kröger-Vink notation with $O_O^\times$, $v_O^{\cdot\cdot}$, and e' denoting regular lattice oxygen (relatively neutral), oxygen vacancy (relatively two-fold positive), and electron (relatively negative), respectively.

$$H_2 + O_O^\times \rightarrow H_2O + v_O^{\cdot\cdot} + 2e' \quad (3)$$

In the second step, these electrons are consumed by reduction of carbon dioxide, which annihilates an oxygen vacancy by donating an oxygen atom to the catalyst, thus forming the second product carbon

monoxide.

$$CO_2 + v_O^{\cdot\cdot} + 2e^{'} \rightarrow O_O^{\times} + CO \quad (4)$$

Both half reactions are coupled by the electron transfer *via* the solid catalyst substrate and thus for the case of steady state conditions, the following relationship for the reaction rate densities *r* holds:

$$r_{H_2-ox} = r_{CO_2-red} = r_{rWGS} \quad (5)$$

Therein, the subscripts "H_2-ox" and "CO_2-red" refer to Eqs. (3) and (4), respectively. Both are equal to the net rate of the rWGS reaction r_{rWGS}, which is compared in a surface area-normalised form (thus called specific activity) in Fig. 2.

As one can see in this figure, upon changing the composition of the investigated perovskite-type catalysts, the reaction rate is improved. In the following, we thus propose a relation between the observed catalyst activities in Fig. 2 and the corresponding catalyst composition based on the characteristics of an assumed MvK-type redox mechanism on mixed conducting perovskites. To do so, it is helpful to first summarize previous results on similar materials:

(i) CO_2 reduction proceeds on the perovskite surface and is only little affected by exsolution of metallic particles [40]. The availability of a sufficiently high concentration of electrons in the electro-catalyst increases efficiency drastically. Thus, the CO_2 reduction rate is higher on more easily reducible oxides [40].

(ii) Exsolved metallic particles can enhance the H_2 oxidation rate significantly [34,47]. The improvement of H_2 oxidation rate occurs by spillover of adsorbed hydrogen species from the metal to the oxide – i.e. the bare oxide surface suffers from a depletion of reactive species, hence here H_2 activation is limiting the net reaction rate, while exsolved metallic particles help sustaining a significant coverage with an active hydrogen species [58].

(iii) Surface enrichment of Sr causes performance degradation of perovskite-type electro-catalysts, but enrichment of La shows only minor effects [59,60].

With this in mind, let us now look at the catalyst performance data in Fig. 2. Doping $LaFeO_3$ with calcium instead of strontium does not visibly change the catalytic activity of the investigated perovskite. This is in agreement with previous results, since both Ca and Sr do not show any redox activity and their effect on defect chemistry (e.g. electron concentration) is only due to their charge.

Changing La against Nd caused an improvement in the specific activity by up to a factor of two (compare the purple and orange curves in Fig. 3). This result is difficult to be unambiguously explained in quantitative terms using the data available so far. However, two potential qualitative explanations shall be briefly discussed here. First, the different redox activity of La and Nd may be the reason for the observed behaviour. While La in the perovskite bulk has only a minor (if any) redox activity, there are indications that surface La actively participates in redox reactions [61]. Assuming a slightly easier reducibility of surface Nd compared to surface La may explain the increased rWGS activity of the Nd-based catalysts *via* improvement of the CO_2 reduction reaction (Eq. (4)). Second, the iron oxide phases observed on $Nd_{0.6}Ca_{0.4}FeO_{3-\delta}$ and $Nd_{0.9}Ca_{0.1}FeO_{3-\delta}$ may contribute to an increased CO_2 reduction rate. Formation of these phases might as well be simply a consequence of the high redox activity of the Nd-containing surface, without a significant enhancing effect of the iron oxide phases on the CO_2 reduction. The exact relations are still to be investigated further. However, any role of FeO and Fe_3O_4 for an improved H_2 oxidation activity can be definitely ruled out as demonstrated in Ref. [58].

A further noteworthy increase of the catalyst performance was achieved by introduction of the reducible elements Co and Ni, which under reaction conditions both caused decoration of the oxide catalysts by metallic precipitates (see Figs. 2 and 6). Hence – by considering the above-mentioned previous results of H_2 oxidation on exsolution-decorated electro-catalysts – we suggest the associated specific activity improvement to be mainly caused by an enhancement of the H_2 oxidation rate (Eq. (3)). Some additional activity enhancement may originate from the easier reducibility and the corresponding higher oxygen vacancy concentration especially of the cobalt doped material.

A summary of both interpretations is sketched in Fig. 9, which shows the job sharing of oxide surface and metal exsolution, catalysing CO_2 reduction and H_2 oxidation, respectively. The connection of both half-reactions is achieved by electrons and oxygen vacancies flowing via the mixed conducting perovskite-type catalyst.

To summarize, the high reactivity of $Nd_{0.6}Ca_{0.4}Fe_{0.9}Co_{0.1}O_{3-\delta}$ (and to some extent $Nd_{0.6}Ca_{0.4}Fe_{0.9}Ni_{0.1}O_{3-\delta}$) can be explained by the synergistic effect of the perovskite host lattice with its capability for high oxygen vacancy concentration, responsible for effective CO_2 activation, the formed CoO (and/or FeO) on the surface, which is contributing to the oxygen chemistry, and the exsolved metal nanoparticles, which are enhancing the H_2 adsorption and dissociation ability of the catalyst surface.

3.6. Deactivation behavior of investigated perovskites

To assess the deactivation behaviour of the investigated perovskites, rWGS reactions at constant high temperatures (600 °C) were conducted. Here, results for $Nd_{0.6}Ca_{0.4}FeO_{3-\delta}$ and Co-doped $Nd_{0.6}Ca_{0.4}Fe_{0.9}Co_{0.1}O_{3-\delta}$ are highlighted in Fig. 10. Results for the other materials are displayed in the supporting info (Figs. S18–S20). To ensure the same well-defined starting point for all experiments, all samples were subjected to an oxidizing pre-treatment at 600 °C for 30 min. Following a cooling down period (to 300 °C in O_2), the reaction gas atmosphere was switched on. A sharp increase of reaction temperature to 600 °C in order to find possible pronounced activation or deactivation effects during reaction onset did not reveal any such effects.

For $Nd_{0.6}Ca_{0.4}FeO_{3-\delta}$ (Fig. 10), a slow deactivation over time was observed which could be seen in the slightly decreasing CO signal. This slow deactivation is very likely attributed to formation of $CaCO_3$ crystallites on the surface, as observed in SEM images and XRD after reaction (Figs. S10 and S4). The $CaCO_3$ is formed in two stages: Ca-segregation to the surface and its reaction with CO_2 from the reaction atmosphere. This phenomenon of carbonate formation is a well-known issue for perovskites with alkaline earth metals as A-site cations, as shown in literature e.g. for $BaCo_{0.4}Fe_{0.4}Zr_{0.2}O_{3-\delta}$ [54]. The formed $CaCO_3$ crystallites are covering part of the perovskite surface, blocking active sites. The slow deactivation is a result of the proceeding growth of $CaCO_3$. Possible strategies for reducing this deactivation process are either a reduction of the Ca-content, the use of an A-site sub-stoichiometric material or a change of the A-site composition to elements that are less prone to segregation or carbonate formation [62]. For the tested perovskites with

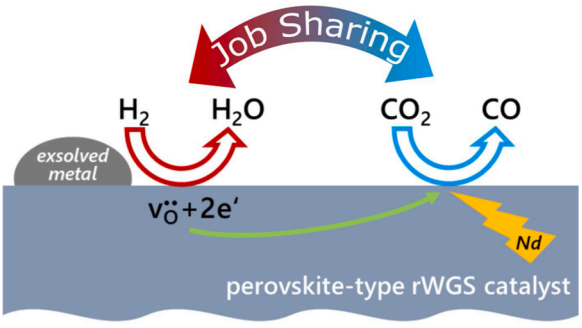

Fig. 9. Sketch of the job sharing during rWGS reaction on the surface of a mixed conducting perovskite decorated with exsolved metallic particles. While the metal enhances mainly the H_2 oxidation rate at the particle/oxide interface, the presence of easier reducible Nd improves at the oxide surface the CO_2 reduction activity. Both steps of the reaction occur at different sites of the catalyst surface.

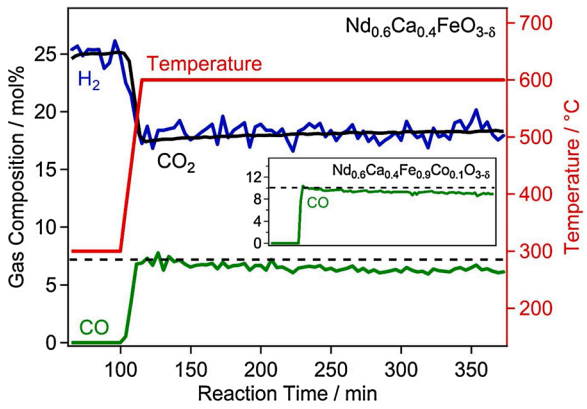

Fig. 10. Isothermal rWGS reaction at 600 °C for $Nd_{0.6}Ca_{0.4}FeO_{3-\delta}$. The initial product gas concentration is indicated with dashed lines. During reaction (about 5 h) the catalyst showed slight deactivation as can be seen in the decreasing CO signal and the increasing amount of H_2. The inset highlights the results for the Co doped material $Nd_{0.6}Ca_{0.4}Fe_{0.9}Co_{0.1}O_{3-\delta}$ where a slight deactivation was observed over time as well.

lower A-site Ca doping, an already reduced tendency for segregation and $CaCO_3$ formation was observed, as shown by XRD and SEM data (Figs. S3/S9 and S5/S11).

$Nd_{0.9}Ca_{0.1}FeO_{3-\delta}$, $La_{0.9}Ca_{0.1}FeO_{3-\delta}$, and $La_{0.6}Ca_{0.4}FeO_{3-\delta}$ showed a similar behaviour with respect to catalytic activity with slow deactivation over time (Figs. S18–S20). For the Co-doped $Nd_{0.6}Ca_{0.4}Fe_{0.9}Co_{0.1}O_{3-\delta}$, the same behaviour was observed as well, see Fig. 10 (inset). In in-situ XRD data (Fig. 5), the formation of $CaCO_3$ was observed above a reaction temperature of 500 °C. With increasing reaction temperature, the corresponding reflex grew more intense, indicating the growth of the $CaCO_3$ crystallites.

4. Conclusions

Six rare earth based perovskite-type oxides were investigated with respect to their rWGS performance, as well as their corresponding surface structure and morphology (using XRD and SEM). The highest catalytic activity was achieved when formation of metallic nanoparticles by exsolution occurred during reaction, as could be shown for the Ni- and Co-doped materials $Nd_{0.6}Ca_{0.4}Fe_{0.9}Ni_{0.1}O_{3-\delta}$ and $Nd_{0.6}Ca_{0.4}Fe_{0.9}Co_{0.1}O_{3-\delta}$. We propose that this is due to a Mars-van-Krevelen-type mechanism of the rWGS reaction on these materials with a highly beneficial job-sharing ability of the metal-particle-decorated catalyst surfaces. On the one hand, dissociative H_2 adsorption takes place on the metal particles. By spillover, the active hydrogen species can subsequently increase the reduction rate (and thus the oxygen vacancy generation rate) in the perovskite backbone compared to the undecorated perovskite. This backbone, on the other hand, is responsible for CO_2 activation. It shows a pronounced defect chemistry, including oxygen vacancies, and can reduce CO_2, accepting one of its O atoms to re-fill a vacancy.

The choice of both A-site and B-site compositions of the perovskite material play an important role for the resulting behaviour and performance. For the design of an optimal catalyst material, several aspects must be considered:

(i) The used rare earth metal on the A-site can – *via* its aptitude to redox behaviour – influence the reducibility of the perovskite backbone and its ability for oxygen vacancy formation. This, in turn, has an effect on the CO_2 reduction rate, but also on the exsolution process (this was also seen in previous work regarding exsolution [43]). In this work, we have shown that exchanging La with the presumably more redox-active Nd increased the catalytic activity for rWGS.

(ii) Doping of the A-site with an alkaline earth metal is important for the perovskite defect chemistry, affecting electronic and ionic conductivity, oxygen vacancy concentration, and thus CO_2 reduction rate and exsolution behaviour. However, alkaline earth metal doping comes with the disadvantage of segregation effects and carbonate formation during rWGS. For our Ca-doped materials, we observed $CaCO_3$ covering the surface, thus blocking active sites and resulting in catalyst deactivation over time. The carbonate formation increased with a higher Ca content and more pronounced B-site metal exsolution.

(iii) Using an easily reducible element (such as Co or Ni) as B-site dopant in combination with a less reducible main component (in our case Fe) not only facilitates formation of metal particles on the surface, but also enables a preferential exsolution of the dopant element (found in this study both for Ni- and Co-doping). At the same time, the less reducible main component ensures that a stable perovskite backbone is retained, because it is not completely reduced under the same conditions. The metal particles strongly increase the catalytic activity for rWGS, as was observed for both the Ni- and the Co-doped material. This stable backbone can provide a good anchoring of exsolved nanoparticles, thus preventing sintering and ensuring a high amount of gas/metal/oxide three-phase boundaries. For our Co-doped material, no sintering of the metal nanoparticles could be observed, even up to 700 °C.

(iv) The choice of the B-site dopant is crucial. Cobalt is known to be highly active for rWGS, and consequently the Co-doped perovskite showed the best rWGS performance. In contrast, Fe particles exsolved by reductive pre-treatment, did not enhance the catalytic activity.

These considerations can be used to tune the perovskite catalyst composition, achieving a material exhibiting excellent catalyst properties – exsolution of catalytically highly active metal nanoparticles with good sintering resistance and optimal size, distribution, and composition from a stable and reducible perovskite backbone, while showing only minimal carbonate formation. Not only changing the used elements and their ratio, but also introducing a sub-stoichiometry to either of the perovskite sites is conceivable, giving an even wider range of possibilities for optimization. Thus, an optimal rWGS performance tuned to the actual process parameters – with a high catalytic activity and stable operation – can be realized.

Our results show that this material class is ideal to meet current challenges for industrial scale rWGS. Moreover, rWGS belongs to the most promising reactions for future CO_2 conversion and utilization systems and belongs to the closest to implementation.

Funding

This project has received funding from the European Research Council (ERC) under the European Union's Horizon 2020 research and innovation programme (grant agreement n° 755744 / ERC - Starting Grant TUCAS).

CRediT authorship contribution statement

L. Lindenthal: Conceptualization, Investigation, Formal analysis, Validation, Writing - original draft, Writing - review & editing. **J. Popovic:** Investigation, Formal analysis. **R. Rameshan:** Data curation, Investigation, Formal analysis. **J. Huber:** Investigation, Formal analysis. **F. Schrenk:** Investigation, Formal analysis. **T. Ruh:** Data curation, Validation, Writing - review & editing. **A. Nenning:** Data curation, Validation. **S. Löffler:** Investigation, Formal analysis. **A.K. Opitz:** Supervision, Validation, Writing - review & editing. **C. Rameshan:** Conceptualization, Funding acquisition, Project administration, Supervision, Writing - original draft, Writing - review & editing.

Declaration of Competing Interest

The authors report no declarations of interest.

Acknowledgement

The X-ray measurements were carried out within the X-Ray Center of TU Wien. The authors acknowledge TU Wien Bibliothek for financial support through its Open Access Funding Programme.

Appendix A. Supplementary data

Supplementary material related to this article can be found, in the online version, at doi:https://doi.org/10.1016/j.apcatb.2021.120183.

References

[1] K.M.K. Yu, I. Curcic, J. Gabriel, S.C.E. Tsang, Recent advances in CO_2 capture and utilization, Chemsuschem 1 (2008) 893–899.
[2] P. Falkowski, R.J. Scholes, E. Boyle, J. Canadell, D. Canfield, J. Elser, N. Gruber, K. Hibbard, P. Hogberg, S. Linder, F.T. Mackenzie, B. Moore, T. Pedersen, Y. Rosenthal, S. Seitzinger, V. Smetacek, W. Steffen, The global carbon cycle: a test of our knowledge of earth as a system, Science 290 (2000) 291–296.
[3] G. Centi, E.A. Quadrelli, S. Perathoner, Catalysis for CO_2 conversion: a key technology for rapid introduction of renewable energy in the value chain of chemical industries, Energy Environ. Sci. 6 (2013) 1711–1731.
[4] Y.A. Daza, J.N. Kuhn, CO_2 conversion by reverse water gas shift catalysis: comparison of catalysts, mechanisms and their consequences for CO_2 conversion to liquid fuels, RSC Adv. 6 (2016) 49675–49691.
[5] C. Rameshan, H. Li, K. Anic, M. Roiaz, V. Pramhaas, R. Rameshan, R. Blume, M. Haevecker, J. Knudsen, A. Knop-Gericke, G. Rupprechter, In situ NAP-XPS spectroscopy during methane dry reforming on ZrO_2/Pt(111) inverse model catalyst, J. Phys. Condensed Matter 30 (2018).
[6] P.M. Mortensen, I. Dybkjaer, Industrial scale experience on steam reforming of CO_2-rich gas, Appl. Catalysis A-General 495 (2015) 141–151.
[7] M. Behrens, Promoting the synthesis of methanol: understanding the requirements for an industrial catalyst for the conversion of CO_2, Angewandte Chem. Int. Ed. 55 (2016) 14906–14908.
[8] T. Riedel, M. Claeys, H. Schulz, G. Schaub, S.S. Nam, K.W. Jun, M.J. Choi, G. Kishan, K.W. Lee, Comparative study of Fischer-Tropsch synthesis with H_2/CO and H_2/CO_2 syngas using Fe- and Co-based catalysts, Appl. Catalysis A-General 186 (1999) 201–213.
[9] J.C. Matsubu, V.N. Yang, P. Christopher, Isolated metal active site concentration and stability control catalytic CO_2 reduction selectivity, J. Am. Chem. Soc. 137 (2015) 3076–3084.
[10] C.A. Galvan, J. Schumann, M. Behrens, J.L.G. Fierro, R. Schlogl, E. Frei, Reverse water-gas shift reaction at the Cu/ZnO interface: influence of the Cu/Zn ratio on structure-activity correlations, Appl. Catalysis B-Environ. 195 (2016) 104–111.
[11] L.H. Wang, H. Liu, Y. Liu, Y. Chen, S.Q. Yang, Effect of precipitants on Ni-CeO_2 catalysts prepared by a co-precipitation method for the reverse water-gas shift reaction, J. Rare Earths 31 (2013) 969–974.
[12] S.E. Collins, J.J. Delgado, C. Mira, J.J. Calvino, S. Bernal, D.L. Chiavassa, M. A. Baltanas, A.L. Bonivardi, The role of Pd-Ga bimetallic particles in the bifunctional mechanism of selective methanol synthesis via CO_2 hydrogenation on a Pd/Ga_2O_3 catalyst, J. Catal. 292 (2012) 90–98.
[13] L.N. Liu, S. Das, T.J. Chen, N. Dewangan, J. Ashok, S.B. Xi, A. Borgna, Z.W. Li, S. Kawi, Low temperature catalytic reverse water-gas shift reaction over perovskite catalysts in DBD plasma, Appl. Catalysis B-Environ. 265 (2020).
[14] L. Pastor-Pérez, F. Baibars, E. Le Saché, H. Arellano-Garcia, S. Gu, T.R. Reina, CO_2 valorisation via Reverse Water-Gas Shift reaction using advanced Cs doped Fe-Cu/Al_2O_3 catalysts, J. Co2 Util. 21 (2017) 423–428.
[15] D.H. Kim, J.L. Park, E.J. Park, Y.D. Kim, S. Uhm, Dopant effect of barium zirconate-based perovskite-type catalysts for the intermediate-temperature reverse water gas shift reaction, ACS Catal. 4 (2014) 3117–3122.
[16] Y.A. Daza, D. Maiti, R.A. Kent, V.R. Bhethanabotla, J.N. Kuhn, Isothermal reverse water gas shift chemical looping on $La_{0.75}Sr_{0.25}Co_{1-y}Fe_yO_3$ perovskite-type oxides, Catal. Today 258 (2015) 691–698.
[17] C.S. Chen, W.H. Cheng, S.S. Lin, Study of reverse water gas shift reaction by TPD, TPR and CO_2 hydrogenation over potassium-promoted Cu/SiO_2 catalyst, Appl. Catalysis a-General 238 (2003) 55–67.
[18] L. Pastor-Pérez, M. Shah, E. le Saché, T.R. Reina, Improving Fe/Al_2O_3 catalysts for the reverse water-gas shift reaction: on the effect of Cs as Activity/Selectivity promoter, Catalysts 8 (2018).
[19] J. Ko, B.K. Kim, J.W. Han, Density functional theory study for catalytic activation and dissociation of CO_2 on bimetallic alloy surfaces, J. Phys. Chem. C 120 (2016) 3438–3447.
[20] D.L. Jurkovic, A. Pohar, V. Dasireddy, B. Likozar, Effect of copper-based catalyst support on reverse water-gas shift reaction (RWGS) activity for CO_2 reduction, Chem. Eng. Technol. 40 (2017) 973–980.
[21] L. Lindenthal, R. Rameshan, H. Summerer, T. Ruh, J. Popovic, A. Nenning, S. Löffler, A.K. Opitz, P. Blaha, C. Rameshan, Modifying the surface structure of perovskite-based catalysts by nanoparticle exsolution, Catalysts 10 (2020) 268.
[22] J. Hwang, R.R. Rao, L. Giordano, Y. Katayama, Y. Yu, Y. Shao-Horn, Perovskites in catalysis and electrocatalysis, Science 358 (2017) 751–756.
[23] Y. Nishihata, J. Mizuki, T. Akao, H. Tanaka, M. Uenishi, M. Kimura, T. Okamoto, N. Hamada, Self-regeneration of a Pd-Perovskite catalyst for automotive emissions control, Nature 418 (2002) 164–167.
[24] O. Kwon, S. Sengodan, K. Kim, G. Kim, H.Y. Jeong, J. Shin, Y.W. Ju, J.W. Han, Exsolution trends and co-segregation aspects of self-grown catalyst nanoparticles in perovskites, Nat. Commun. 8 (2017).
[25] D. Neagu, G. Tsekouras, D.N. Miller, H. Menard, J.T.S. Irvine, In situ growth of nanoparticles through control of non-stoichiometry, Nat. Chem. 5 (2013) 916–923.
[26] D. Papargyriou, J.T.S. Irvine, Nickel nanocatalyst exsolution from (La,Sr) (Cr,M,Ni) O_3 (M=Mn,Fe) perovskites for the fuel oxidation layer of Oxygen Transport Membranes, Solid State Ion. 288 (2016) 120–123.
[27] Q. Zhao, H. Lorenz, S. Turner, O.I. Lebedev, G. Van Tendeloo, C. Rameshan, B. Klotzer, J. Konzett, S. Penner, Catalytic characterization of pure SnO_2 and GeO_2 in methanol steam reforming, Appl. Catalysis A-General 375 (2010) 188–195.
[28] D. Neagu, T.S. Oh, D.N. Miller, H. Menard, S.M. Bukhari, S.R. Gamble, R.J. Gorte, J.M. Vohs, J.T.S. Irvine, Nano-socketed nickel particles with enhanced coking resistance grown in situ by redox exsolution, Nat. Commun. 6 (2015).
[29] T.S. Oh, E.K. Rahani, D. Neagu, J.T.S. Irvine, V.B. Shenoy, R.J. Gorte, J.M. Vohs, Evidence and model for strain-driven release of metal nanocatalysts from perovskites during exsolution, J. Phys. Chem. Lett. 6 (2015) 5106–5110.
[30] E. le Saché, L. Pastor-Pérez, D. Watson, A. Sepúlveda-Escribano, T.R. Reina, Ni stabilised on inorganic complex structures: superior catalysts for chemical CO_2 recycling via dry reforming of methane, Appl. Catalysis B-Environ. 236 (2018) 458–465.
[31] M.A. Naeem, P.M. Abdala, A. Armutlulu, S.M. Kim, A. Fedorov, C.R. Müller, Exsolution of metallic Ru nanoparticles from defective, fluorite-type solid solutions $Sm_2Ru_xCe_{2-x}O_7$ to impart stability on dry reforming catalysts, ACS Catal. 10 (2020) 1923–1937.
[32] C. Tsounis, Y. Wang, H. Arandiyan, R.J. Wong, C.Y. Toe, R. Amal, J. Scott, Tuning the selectivity of $LaNiO_3$ perovskites for CO_2 hydrogenation through potassium substitution, Catalysts 10 (2020).
[33] D. Neagu, V. Kyriakou, I.L. Roiban, M. Aouine, C.Y. Tang, A. Caravaca, K. Kousi, I. Schreur-Piet, I.S. Metcalfe, P. Vernoux, M.C.M. van de Sanden, M.N. Tsampas, In situ observation of nanoparticle exsolution from perovskite oxides: from atomic scale mechanistic insight to nanostructure tailoring, ACS Nano 13 (2019) 12996–13005.
[34] A.K. Opitz, A. Nenning, C. Rameshan, R. Rameshan, R. Blume, M. Haevecker, A. Knop-Gericke, G. Rupprechter, J. Fleig, B. Kloetzer, Enhancing electrochemical water-splitting kinetics by polarization-driven formation of near-surface Iron(0): an in situ XPS study on perovskite-type electrodes, Angewandte Chem. Int. Ed. 54 (2015), 2628-+.
[35] T. Gotsch, N. Kopfle, M. Grunbacher, J. Bernardi, E.A. Carbonio, M. Havecker, A. Knop-Gericke, M.F. Bekheet, L. Schlicker, A. Doran, A. Gurlo, A. Franz, B. Klotzer, S. Penner, Crystallographic and electronic evolution of lanthanum strontium ferrite ($La_{0.6}Sr_{0.4}FeO_{3-\delta}$) thin film and bulk model systems during iron exsolution, J. Chem. Soc. Faraday Trans. 21 (2019) 3781–3794.
[36] ICDD, PDF-4+ 2019, in: S. Kabekkodu (Ed.), International Centre for Diffraction Data, Newtown Square, PA, USA, 2018.
[37] J. Popovic, L. Lindenthal, R. Rameshan, T. Ruh, A. Nenning, S. Löffler, A.K. Opitz, C. Rameshan, High temperature water gas shift reactivity of novel perovskite catalysts, Catalysts 10 (2020) 582.
[38] D.H. Kim, S.W. Han, H.S. Yoon, Y.D. Kim, Reverse water gas shift reaction catalyzed by Fe nanoparticles with high catalytic activity and stability, J. Ind. Eng. Chem. 23 (2015) 67–71.
[39] L.H. Wang, H. Liu, Y. Chen, S.Q. Yang, Reverse water-gas shift reaction over co-precipitated Co-CeO_2 catalysts: effect of Co content on selectivity and carbon formation, Int. J. Hydrogen Energy 42 (2017) 3682–3689.
[40] A.K. Opitz, A. Nenning, C. Rameshan, M. Kubicek, T. Goetsch, R. Blume, M. Haevecker, A. Knop-Gericke, G. Rupprechter, B. Kloetzer, J. Fleig, Surface chemistry of perovskite-type electrodes during high temperature CO_2 electrolysis investigated by Operando photoelectron spectroscopy, ACS Appl. Mater. Interfaces 9 (2017) 35847–35860.
[41] H. Ban, C. Li, K. Asami, K. Fujimoto, Influence of rare-earth elements (La, Ce, Nd and Pr) on the performance of Cu/Zn/Zr catalyst for CH_3OH synthesis from CO_2, Catal. Commun. 54 (2014) 50–54.
[42] W. Lee, J.W. Han, Y. Chen, Z. Cai, B. Yildiz, Cation size mismatch and charge interactions drive dopant segregation at the surfaces of manganite perovskites, J. Am. Chem. Soc. 135 (2013) 7909–7925.
[43] L. Lindenthal, T. Ruh, R. Rameshan, H. Summerer, A. Nenning, C. Herzig, S. Loffler, A. Limbeck, A.K. Opitz, P. Blaha, C. Rameshan, Ca-doped rare earth perovskite materials for tailored exsolution of metal nanoparticles, Acta Crystallographica Section B 76 (2020) 1055–1070.
[44] R. Andoulsi, K. Horchani-Naifer, M. Ferid, Structural and electrical properties of calcium substituted lanthanum ferrite powders, Powder Technol. 230 (2012) 183–187.
[45] G.S. Yablonsky, R. Pilasombat, J.P. Breen, R. Burch, S. Hengrasmee, Cycles across an equilibrium: a kinetic investigation of the reverse and forward WGS reaction over a 2% Pt/CeO_2 catalyst (Experimental data and qualitative interpretation), Chem. Eng. Sci. 65 (2010) 2325–2332.

[46] M.D. Porosoff, X.F. Yang, J.A. Boscoboinik, J.G.G. Chen, Molybdenum carbide as alternative catalysts to precious metals for highly selective reduction of CO_2 to CO, Angewandte Chem. Int. Ed. 53 (2014) 6705–6709.
[47] G. Tsekouras, D. Neagu, J.T.S. Irvine, Step-change in high temperature steam electrolysis performance of perovskite oxide cathodes with exsolution of B-site dopants, Energy Environ. Sci. 6 (2013) 256–266.
[48] D. Maiti, Y.A. Daza, M.M. Yung, J.N. Kuhn, V.R. Bhethanabotla, Oxygen vacancy formation characteristics in the bulk and across different surface terminations of $La_{1-x}Sr_xFe_{1-y}Co_yO_{3-\delta}$ perovskite oxides for CO2 conversion, J. Mater. Chem. A 4 (2016) 5137–5148.
[49] A. Goguet, F.C. Meunier, D. Tibiletti, J.P. Breen, R. Burch, Spectrokinetic investigation of reverse water-gas-shift reaction intermediates over a Pt/CeO_2 catalyst, J. Phys. Chem. B 108 (2004) 20240–20246.
[50] D.J. Pettigrew, D.L. Trimm, N.W. Cant, The effects of rare-earth-oxides on the reverse water-gas shift reaction on palladium alumina, Catal. Letters 28 (1994) 313–319.
[51] B.W. Lu, K. Kawamoto, Preparation of mesoporous CeO_2 and monodispersed NiO particles in CeO2, and enhanced selectivity of NiO/CeO_2 for reverse water gas shift reaction, Mater. Res. Bull. 53 (2014) 70–78.
[52] P. Steiger, M. Nachtegaal, O. Krocher, D. Ferri, Reversible Segregation of Ni in $LaFe_{0.8}Ni_{0.2}O_{3+/-\delta}$During Coke Removal, Chemcatchem 10 (2018) 4456–4464.
[53] H.A. Wriedt, The Fe-O (Iron-Oxygen) System, J. Phase Equilibria Diffus. 12 (1991) 170–200.
[54] K. Efimov, O. Czuprat, A. Feldhoff, In-situ X-ray diffraction study of carbonate formation and decomposition in perovskite-type BCFZ, J. Solid State Chem. 184 (2011) 1085–1089.
[55] S.B. Adler, Chemical expansivity of electrochemical ceramics, J. Am. Ceram. Soc. 84 (2001) 2117–2119.
[56] Y.A. Daza, R.A. Kent, M.M. Yung, J.N. Kuhn, Carbon dioxide conversion by reverse water-gas shift chemical looping on perovskite-type oxides, Ind. Eng. Chem. Res. 53 (2014) 5828–5837.
[57] C. Doornkamp, V. Ponec, The universal character of the Mars and Van Krevelen mechanism, J. Mol. Catalysis a-Chem. 162 (2000) 19–32.
[58] A.K. Opitz, A. Nenning, V. Vonk, S. Volkov, F. Bertram, H. Summerer, S. Schwarz, A. Steiger-Thirsfeld, J. Bernardi, A. Stierle, J. Fleig, Understanding electrochemical switchability of perovskite-type exsolution catalysts, Nat. Commun. 11 (2020).
[59] Y. Chen, H. Tellez, M. Burriel, F. Yang, N. Tsvetkov, Z.H. Cai, D.W. McComb, J. A. Kilner, B. Yildiz, Segregated chemistry and structure on (001) and (100) surfaces of $(La_{1-x}Sr_x)_2CoO_4$ override the crystal anisotropy in oxygen exchange kinetics, Chem. Mater. 27 (2015) 5436–5450.
[60] J. Druce, H. Tellez, M. Burriel, M.D. Sharp, L.J. Fawcett, S.N. Cook, D.S. McPhail, T. Ishihara, H.H. Brongersma, J.A. Kilner, Surface termination and subsurface restructuring of perovskite-based solid oxide electrode materials, Energy Environ. Sci. 7 (2014) 3593–3599.
[61] L. Qin, M.Q. Guo, Z. Cheng, M.Y. Xu, Y. Liu, D.K. Xu, J.A. Fan, L.S. Fan, Improved cyclic redox reactivity of lanthanum modified iron-based oxygen carriers in carbon monoxide chemical looping combustion, J. Mater. Chem. A 5 (2017) 20153–20160.
[62] H. Kwon, W. Lee, J.W. Han, Suppressing cation segregation on lanthanum-based perovskite oxides to enhance the stability of solid oxide fuel cell cathodes, RSC Adv. 6 (2016) 69782–69789.